PAPER

Temperature-dependent growth mechanisms of low-dimensional ZnO nanostructures

Qijin Cheng and Kostya (Ken) Ostrikov*

One-dimensional ZnO nanostructures were successfully synthesized on single-crystal silicon substrates *via* a simple thermal evaporation and vapour-phase transport method under different process temperatures from 500 to 1000 °C. The detailed and in-depth analysis of the experimental results shows that the growth of ZnO nanostructures at process temperatures of 500, 800, and 1000 °C is governed by different growth mechanisms. At a low process temperature of 500 °C, the ZnO nanostructures feature flat and smooth tips, and their growth is primarily governed by the vapour-solid mechanism. At an intermediate process temperature of 800 °C, the ZnO nanostructures feature cone-shape tips, and their growth is primarily governed by the self-catalyzed and saturated vapour–liquid–solid mechanism. At a high process temperature of 1000 °C, the alloy tip appears on the front side of the ZnO nanostructures, and their growth is primarily governed by the common catalyst-assisted vapour–liquid–solid mechanism. It is also shown that the morphological, structural, optical, and compositional properties of the synthesized ZnO nanostructures are closely related to the process temperature. These results are highly relevant to the development of light-emitting diodes, chemical sensors, energy conversion devices, and other advanced applications.

1. Introduction

Quasi-one-dimensional metal oxide nanostructures such as nanowires, nanobelts, nanorods as well as nanorings have recently been in the spotlight of extensive research efforts.[1–6] This is attributed to their outstanding electrical, optical, physical, chemical, mechanical properties and a broad range of advanced applications including chemical sensors, piezoelectric transducers, energy conversion devices, field-effect transistors, light-emitting diodes, biomedicine and several others.[1–6] Among the quasi-one-dimensional metal oxide nanostructures, one-dimensional ZnO nanostructures have been most extensively studied because of their wide direct band gap of 3.37 eV and a large exciton binding energy of 60 meV.[7,8]

Diverse morphologies of one-dimensional ZnO nanostructures including nanowires, nanocombs, nanotubes, nanorings, nanospheres, nanocages, nanobelts, nanocones, nanotips, nanorods, tetrapods, *etc.* have been produced.[9–13] Moreover, several fabrication techniques have been developed to deposit one-dimensional ZnO nanostructures. These techniques include thermal evaporation and vapour-phase transport, pulsed laser-assisted chemical vapour deposition, metalorganic vapour-phase epitaxial growth, hydrothermal synthesis, template-assisted synthesis, *etc.*[9,12–17] Among them, thermal chemical vapour deposition is widely used due to its simplicity, low cost, and easy operation.

Despite numerous publications on the synthesis and growth mechanisms of low-dimensional ZnO nanostructures, there are still many controversies about the underlying mechanisms for the growth of one-dimensional ZnO nanostructures; the understanding of the growth mechanisms of low-dimensional ZnO nanostructures is still far from completion. For example, when a Au catalyst is used in the synthesis of ZnO nanostructures, some authors observed that the alloy droplet stayed at the tip while others did not find anything at the tip.[9,18] Another perplexing instance is that different growth mechanisms including catalyst-assisted vapour–liquid–solid (VLS), self-catalyzed and saturated VLS, and vapour–solid (VS) mechanisms have been proposed to explain the growth of one-dimensional ZnO nanostructures.[10,14] In the specific process, which growth mechanism dominates? Therefore, detailed and clear understanding of the growth mechanisms of one-dimensional ZnO nanostructures is required to control the morphology, crystallinity, shape, aspect ratio, preferential growth direction, and composition of one-dimensional ZnO nanostructures in an effective and smart way.

In this work, using a simple thermal evaporation and vapour-phase transport deposition technique, we show that the aforementioned three growth mechanisms coexist in the growth of one-dimensional ZnO nanostructures and the dominant one is determined by the subtle change of the experimental conditions. Moreover, the evolution of the surface morphology and the

Plasma Nanoscience Centre Australia (PNCA), CSIRO Materials Science and Engineering, P.O. Box 218, Lindfield, NSW, 2070, Australia. E-mail: Kostya.Ostrikov@csiro.au; Fax: +61-2-94137200; Tel: +61-2-94137634

variation of structural, optical, and compositional properties of the synthesized ZnO nanostructures are extensively investigated using a broad range of advanced characterization tools, including scanning electron microscopy (SEM), transmission electron microscopy (TEM), high resolution transmission electron microscopy (HRTEM), X-ray diffraction (XRD), X-ray photoelectron spectroscopy (XPS), photoluminescence (PL) spectroscopy, etc.

This paper is structured as follows. In Section 2, we present the details of the experimental method and the characterization techniques. The results on the effect of the process temperature of the horizontal tube furnace on the morphological, structural, optical, and compositional properties of the one-dimensional ZnO nanostructures are presented in Section 3. Section 4 is focused on the discussion of the possible growth mechanisms that explain the obtained experimental results in Section 3. The paper ends with a short summary in Section 5.

2. Experimental details

The synthesis of one-dimensional ZnO nanostructures was carried out using a thermal evaporation and vapour-phase transport method in a conventional single-zone horizontal quartz tube furnace (inner diameter 50 mm, length 90 cm). A high-purity Zn powder (Alfa Aesar, −100 mesh, 99.9%) and oxygen gas (99.999%) were used as precursors of Zn and oxygen species, respectively. About 1 g Zn powder contained in an alumina boat was placed at the center of the quartz tube and the set temperature of the furnace was varied from 500 to 1000 °C (referred to as the process temperature in the following text). Si(100) wafers pre-coated with an ~30 nm sputtered gold film were used as substrates. These substrates were positioned approximately 8 cm downstream from the tube center. When the system was evacuated to about 10^{-2} Torr through the use of a rotary pump, an Ar flow of 50 standard cubic centimetres per minute (sccm) was introduced into the system. Then the temperature of the furnace was increased to the desired temperature and the oxygen flow of 5 sccm (10% of argon gas flow) was let into the system and maintained for 30 min. After that, the oxygen flow was discontinued and the system was cooled to ambient temperature under the same Ar flow. After the reaction, the substrate surfaces were covered with a white or gray layer.

The synthesized samples were characterized by XRD, SEM, TEM, HRTEM, PL spectroscopy, and XPS techniques. The crystalline structure of the synthesized samples was investigated using a Philips X'Pert Pro MPD X-ray diffractometer, operated in a locked-couple mode, wherein the incident X-ray wavelength was 1.54 Å (Cu Kα line) at 45 kV and 40 mA. The top-view imaging of the samples was performed using a Zeiss Ultra Plus field emission scanning electron microscope operated at 2 kV. The TEM and HRTEM measurements were undertaken by Philips CM120 Biofilter (operated at 120 kV) and JEOL 3000F (operated at 300 kV) transmission electron microscopes, respectively. PL measurements were carried out by Renishaw inVia micro-Raman System using a 325 nm He–Cd laser for excitation. The chemical composition and bonding states of the synthesized ZnO nanostructures were studied ex situ by a VG ESCALAB 220i-XL X-ray photoelectron spectrometer using a Mg Kα (1253.6 eV) X-ray source at a resolution of 0.6 eV. The

electron spectrometer was calibrated by assuming that the binding energy of the C 1s line is 284.5 eV. All the spectra of the samples were fitted with Gaussian functions after removing the background using the Shirley subtraction method. The elemental composition of the specimens was calculated using:

$$X(\text{at}\%) = \frac{(A_X/S_X)}{\sum\limits_{i=1}^{N}(A_i/S_i)} \times 100\%,$$

where X is the type of the element, A_X is the area under the peak of the element X in the spectrum, and S_X is the sensitivity factor.[19]

3. Results

The crystallinity and crystallographic phases of the synthesized ZnO nanostructures were studied by XRD. Fig. 1 shows the XRD spectra of the samples synthesized at process temperatures of 500, 800, and 1000 °C, respectively. The diffraction peaks in the spectra can be indexed as the hexagonal wurtzite structure of bulk ZnO.[8,15] The lattice parameters for the ZnO sample deposited at a process temperature of 1000 °C are $a = b = 3.246$ Å, and $c = 5.200$ Å. These values are rather close to those of bulk ZnO ($a = b = 3.249$ Å, $c = 5.206$ Å), suggesting that the synthesized ZnO features a high crystal quality. Additionally, a small diffraction peak at $2\theta = 33°$ appearing in the spectrum for the sample deposited at a process temperature of 500 °C is attributed to the (002) crystal plane of Si substrates. No diffraction peaks from other impurities such as metallic zinc and gold were found. Moreover, with the increase of the process temperature, the intensities of all the diffraction peaks significantly increase while the full widths at half maximum of all the diffraction peaks decrease, implying that the crystallinity is improved at a higher process temperature. This is possibly attributed to the higher mobility of the adsorbed species at a higher process temperature.[20,21]

The surface morphology of the synthesized ZnO nanostructures was investigated by SEM. Fig. 2 shows the typical top-view, low- and high-magnification images of low-dimensional ZnO nanostructures synthesized at process temperatures of 500, 800, and 1000 °C, respectively. One can observe that, at a low temperature of 500 °C, ZnO nanostructures are in the nanowire form, while at temperatures of 800 and 1000 °C, ZnO grows in the form of nanobelts. The diameter and length of the ZnO nanowires synthesized at 500 °C are ~35 and ~440 nm, respectively, and the tip is flat (which will also be confirmed by the following TEM measurements). At the process temperature of 800 °C, the (base) width and length of the ZnO nanobelts are ~8.4 and ~28 μm, respectively, and the tip features a conical shape. With a further increase of the process temperature to 1000 °C, the length of the ZnO nanobelts increases to ~50 μm while the width decreases to ~5 μm. Moreover, it is obvious that there is an alloy tip in the growth front. It is noteworthy that the aspect ratio initially shows a rapid decrease from ~12.5 to ~3.3 with the increase of the process temperature from 500 to 800 °C, and then increases to ~10 at the process temperature of 1000 °C.

The structure of the synthesized ZnO nanostructures has also been studied by TEM and HRTEM measurements. Fig. 3
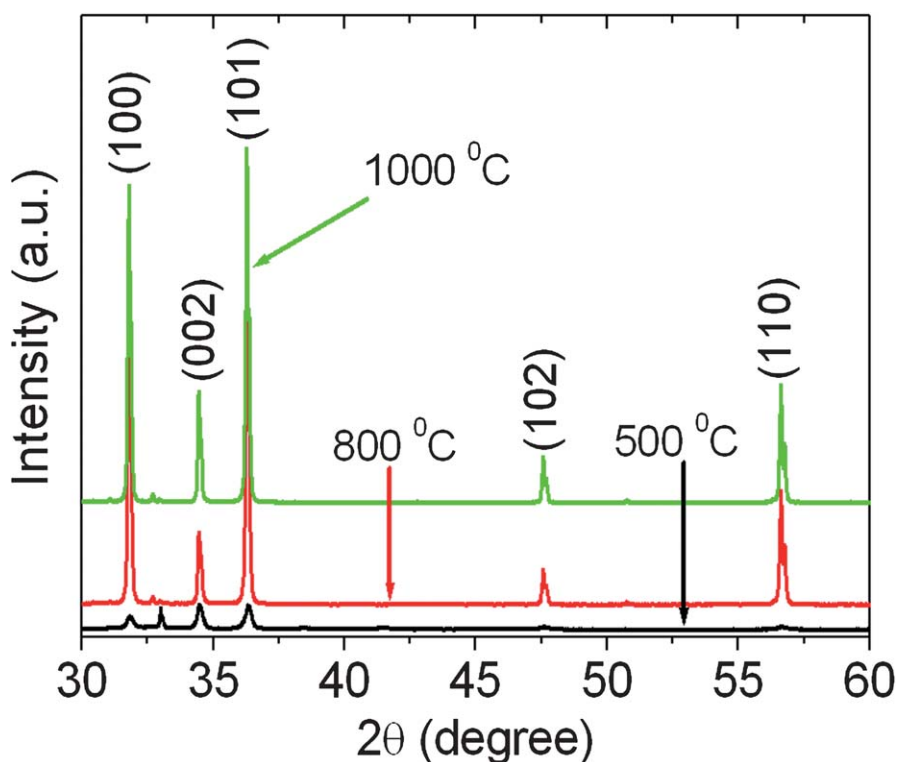
Fig. 1 XRD spectra of the ZnO samples synthesized at process temperatures of 500, 800, and 1000 °C, respectively.
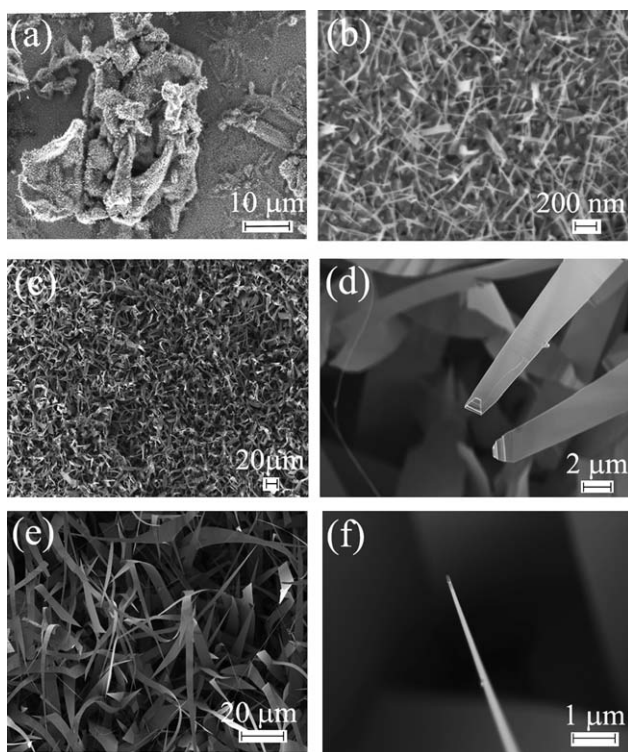

Fig. 2 Typical top-view low- and high-magnification scanning electron micrographs of low-dimensional ZnO nanostructures synthesized at process temperatures of 500 °C (a and b), 800 °C (c and d), and 1000 °C (e and f), respectively.

displays the TEM images of the individual ZnO nanowires or nanobelts prepared at process temperatures of 500, 800, and 1000 °C, respectively. The tips of the nanostructures can be clearly viewed. At a process temperature of 500 °C, the tip of the nanowire is smooth and flat, and the diameter of the nanowire is uniform along the wire. At a process temperature of 800 °C, the tip of the nanobelt has a conical shape and its diameter gradually decreases from the base to the tip. Likewise, at a process temperature of 1000 °C, an alloy droplet appears on the front side of the nanobelt. The TEM results are consistent with the SEM analysis.

Fig. 4(a) shows a typical HRTEM image of the ZnO nanostructures synthesized at a process temperature of 1000 °C. One can notice that clear and well-resolved lattice fringes appear in the image. The interplanar spacing determined from this image is equal to 0.260 nm. This lattice spacing is attributed to the (0002) crystal plane of hexagonal ZnO, suggesting that the ZnO nanostructures grow along the [0001] orientation. The corresponding selected area electron diffraction (SAED) pattern is displayed in Fig. 4(b). The detailed analysis of Fig. 4(b) further confirms that ZnO nanostructures have a single-crystalline hexagonal structure and grow along the *c*-axis direction. It is noteworthy that the crystal defects such as stacking faults or screw dislocations are not observed in the ZnO nanostructures. The preferential growth along the [0001] direction has frequently been observed in the synthesis of ZnO nanostructures.[10,11] This is attributed to the extremely anisotropic crystal structure of ZnO. That is to say, the polar (0002) crystal plane of ZnO has a high surface energy, and therefore experiences the fastest growth and acts as the growth front.[10,11]
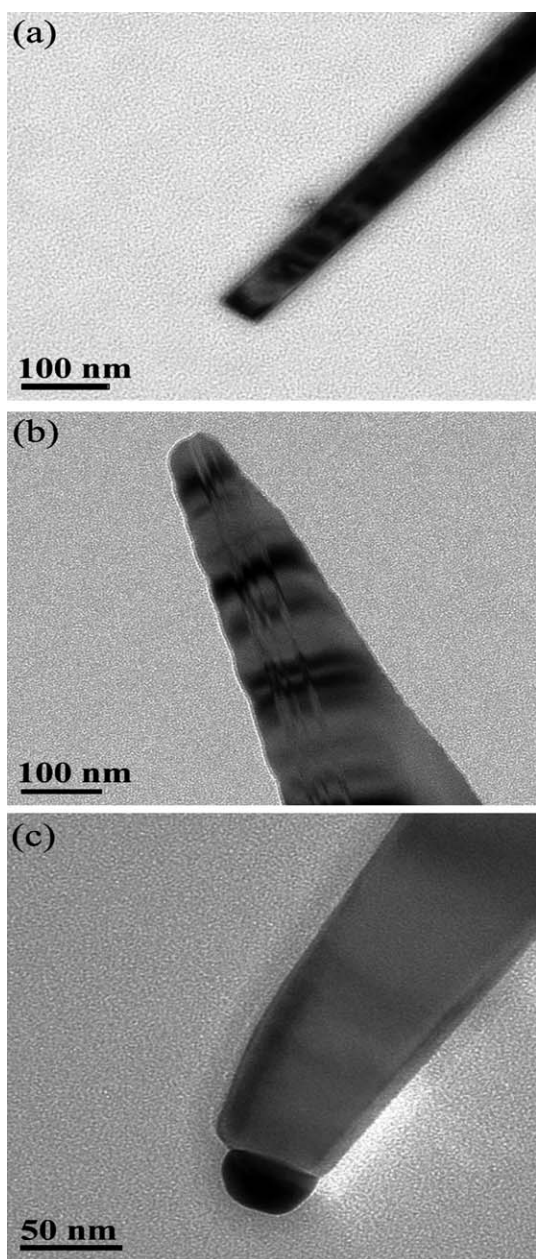
Fig. 3 TEM images of the individual ZnO nanowires or nanobelts prepared at process temperatures of 500 °C (a), 800 °C (b), and 1000 °C (c), respectively.

Fig. 4 A typical HRTEM image and the corresponding selected area electron diffraction (SAED) pattern of the ZnO nanostructures synthesized at a process temperature of 1000 °C.

Fig. 5 (a) PL spectra of the ZnO samples deposited at various process temperatures; (b) the ratio of the intensities of the UV and green peaks (designated as I_{UV}/I_{Green}) as a function of the process temperature.

The optical properties of the synthesized ZnO nanostructures were investigated by photoluminescence spectroscopy. Fig. 5(a) shows the PL spectra of the samples deposited at various process temperatures. Two distinct emissions can be clearly observed: one is sharp ultraviolet emission at ~383 nm, and the other one is broad green emission at ~540 nm. The peak at ~383 nm is generally ascribed to near-band-edge emission, originated from the free-exciton recombination, whereas the peak at ~540 nm is generally attributed to the deep-level defect recombination.[8,22] These deep-level defects presumably originate from the single ionized oxygen vacancies or zinc interstitials, *etc.* An important criterion to evaluate the quality of the synthesized ZnO nanostructures is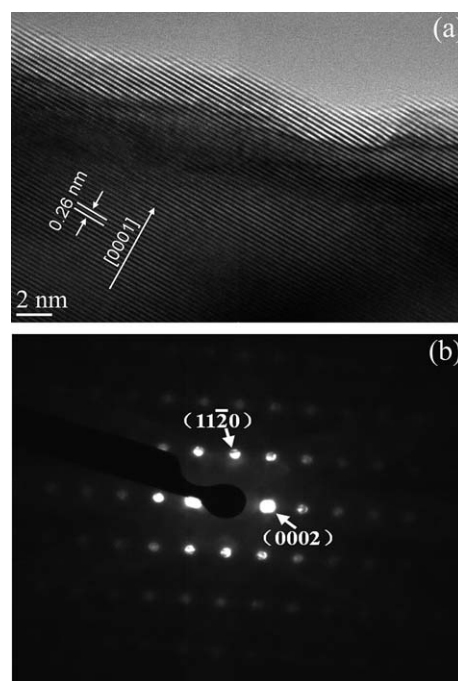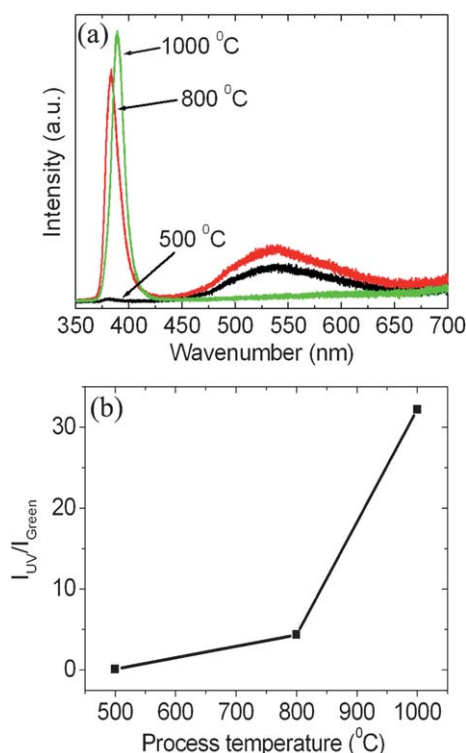 to check the ratio of the intensities of the UV and green peaks.[8,22] Fig. 5(b) displays the ratio of the intensity of the UV peak to that of the green peak (designated as I_{UV}/I_{Green}) as a function of the process temperature. One can notice that the

ratio of the intensities of the UV and green peaks shows a rapid increase in an almost exponential fashion. This indicates that the quality of the synthesized ZnO nanostructures is significantly improved at higher process temperatures. It is worth emphasizing that at a process temperature of 1000 °C, the defect emission-related peak is negligible, suggesting that this material is of a good quality suitable for applications in optoelectronic devices, *etc.*

The elemental composition and bonding states of the synthesized ZnO nanostructures were investigated by XPS. Fig. 6(a–f) show the typical narrow scan XPS spectra of O 1s (a, c, and e) and Zn $2p_{3/2}$ (b, d, and f) of the samples synthesized at the process temperatures of 500, 800, and 1000 °C, respectively. The peak fitting performed on the O 1s spectra (a, c, and e) yields two peaks with the binding energies of 530.2 eV (O_1) and 532.0 eV (O_2).[23,24] These two binding energies can be assigned to O–Zn and O–H bonds, respectively. The occurrence of the O_2 peak in the spectra presumably originates from the surface contamination such as chemisorbed oxygen caused by surface hydroxyl groups. Likewise, the peak fitting on the Zn $2p_{3/2}$ spectra (b, d, and f) yields only one peak located at the binding energy of 1021.5 eV, which is attributed to the Zn–O bonds.[23,25]

Relative atomic concentrations of each element constituting ZnO nanostructures were calculated using the integrated areas of O_1 and Zn $2p_{3/2}$, and corresponding sensitivity factors (Zn: 2.768, O: 0.733). Fig. 7 presents the atomic concentration of oxygen in the synthesized ZnO nanostructures as a function of the process temperature. One can notice that with the increase of the process temperature, the atomic concentration of oxygen increases in an almost linear way, suggesting that the crystal quality of the ZnO
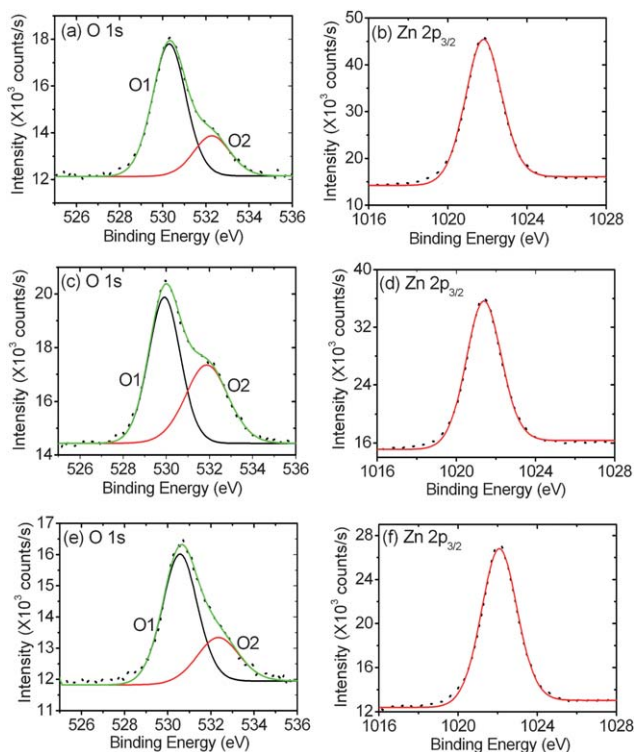

Fig. 7 Atomic concentration of oxygen in the synthesized ZnO nanostructures as a function of the process temperature. At higher process temperatures, the oxygen concentration in the ZnO nanostructures reaches the stoichiometric level.

nanostructures is improved (lower oxygen deficiency at higher process temperatures). In particular, at a process temperature of 1000 °C, the atomic concentration ratio of oxygen to zinc is quite close to unity. The XPS results agree very well with the analysis performed by XRD and PL spectroscopy.

4. Discussion

On the basis of the experimental results observed above, we surmise that the growth of ZnO nanostructures at different process temperatures is governed by different physical mechanisms:

(1) At the process temperature of 500 °C, the growth of ZnO nanowires is primarily governed by the VS mechanism (shown in Fig. 8(a)). This is because no alloy tip can be observed at the front side (only flat and smooth surface is observed). In a typical VS process, the incorporation of gaseous species into the solid

Fig. 6 Typical narrow scan XPS spectra of O 1s (a, c, and e) and Zn $2p_{3/2}$ (b, d, and f) of the ZnO samples synthesized at process temperatures of 500, 800, and 1000 °C, respectively.
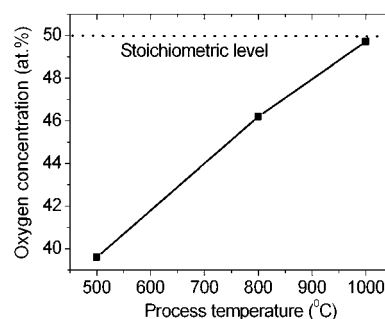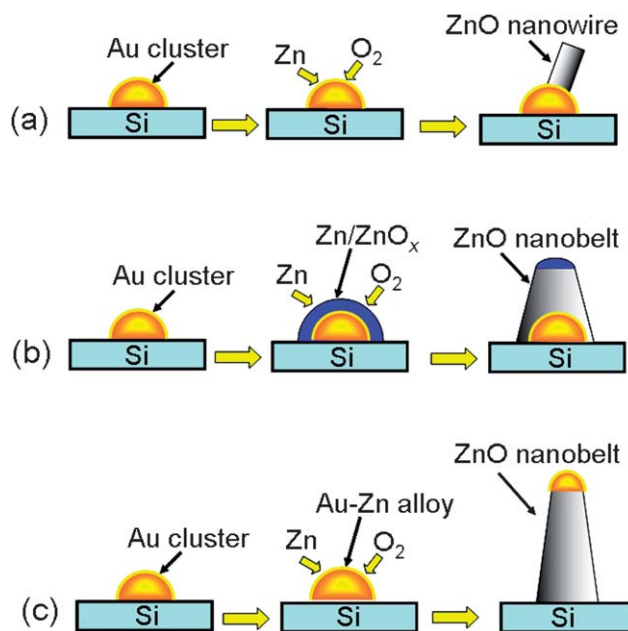

Fig. 8 Temperature-dependent growth mechanisms of the ZnO nanostructures synthesized at the process temperatures of 500 °C (a), 800 °C (b), and 1000 °C (c), respectively.

phase involves the incidence of gaseous species onto the solid surface followed by surface diffusion and capture of the diffusion species by certain sites on the solid surface.[26–28] It has previously been proposed that the growth temperature and gas-phase supersaturation determine the growth rates of the surface planes and the final morphology of the crystals, with other experimental parameters playing less important roles in the VS process.[11] Low supersaturation promotes nanowires or whiskers growth while high supersaturation causes larger crystals to be formed. In the case of our interest, the low process temperature of 500 °C (the melting point of zinc is about 419 °C) ensures that the supersaturation of zinc is low, and therefore promotes nucleation, precipitation, and growth of ZnO nanowires. It is worthwhile to mention that in this case, the Au particles mainly provide a low surface-energy interface and act as preferential adsorption sites for the collection of zinc and oxygen gaseous species. The role of the gold particles as a low surface-energy interface has also been observed in the growth of InAs nanowires by low-pressure metalorganic vapour phase epitaxy.[29]

(2) At the process temperature of 800 °C, the self-catalyzed and saturated VLS mechanism (shown in Fig. 8(b)) plays an essential role in the growth of ZnO nanobelts. This is because the sharp cone-shape tip, characteristic to the self-catalyzed and saturated VLS growth of ZnO nanostructures, has been observed in the SEM and TEM images.[23,30] In this process, the zinc and zinc suboxides (ZnO_x, $x < 1$) liquid droplets are initially formed on the Au-catalyzed Si substrates. These liquid droplets enhance the absorption and diffusion of zinc oxide species at the tips of the ZnO nanostructures during the growth process. With further oxidizing of the liquid droplets, the concentration of oxygen in the droplets increases and subsequent supersaturation of ZnO leads to the segregation of ZnO and growth of ZnO nanostructures. Therefore, the formation of cone-shape tips is attributed to the gradual oxidizing and shrinkage of the Zn/ZnO_x liquid droplets on the top.

(3) At the process temperature of 1000 °C, the growth of ZnO nanobelts is mainly governed by the gold-assisted VLS mechanism (shown in Fig. 8(c)). This is because the alloy nanoparticle has clearly been observed on the nanobelt tip. In the typical VLS process, a Au–Zn liquid alloy is formed during the initial stage. This alloy can serve as a preferential sink to receive the gas-phase precursors and guide the nanostructure growth, still remaining at the growth front of each one-dimensional nanostructure. Subsequently, Zn supersaturation in the liquid alloy leads to strong Zn precipitation at the interface between the droplets and the substrate, Zn oxidation and eventually epitaxial growth of ZnO nanowries.[9]

Since the process temperature of 1000 °C is much higher than the melting point of zinc, there should exist a large amount of zinc vapour in the tube furnace. Indeed, we observed that the pressure inside the furnace increased significantly when the process temperature reached 1000 °C. The significantly increased pressure and a much higher consumption of Zn powder indicated that the Zn vapour pressure also increased quite significantly. Thereby, besides the growth in the [0001] direction, revealed in the HRTEM micrographs, the excess Zn atoms without being dissolved by gold nanoparticles could also attach to the side faces of ZnO nanostructures. This can in turn promote secondary nucleation and growth of ZnO nanostructures, leading to the

two-dimensional growth mode and the eventual formation of the ZnO nanobelts.[31]

It is important to stress that the effects of gas/surface temperature and Zn vapour pressure (supersaturation) in the zinc and oxygen gas phase act concurrently and to some extent, synergistically. This is why it is quite difficult to identify the dominant factor. However, the pronounced secondary nucleation indicates on the significant role of the increased pressure of the Zn vapour pressure. Further studies are required to elucidate the specifics of the growth mechanism.

It has also been found that the width of the ZnO nanobelts shows gradual shrinkage from the base to the tip. The shrinkage of the width of the ZnO nanobelts in this case can be attributed to the surface migration and incorporation of the gold atoms into the ZnO nanostructures, or evaporation of the gold atoms from the ZnO nanostructures at a high process temperature of 1000 °C.[32,33] This process leads to the reduction of Au nanoparticles in size, and as a result, the Si monolayers that nucleate under them also decrease.

Finally, it is worthwhile to mention that, in the vapour-phase growth of nanostructures, the VLS and VS growth mechanisms often compete with each other and the dominant one is determined by the subtle changes of the external experimental conditions.[11,31,34–36] These external experimental conditions include the process temperature at the source materials, gas flow rates of carrier and reactive gases, gas-phase supersaturation, inner diameter of the tube furnace, the distance between the source materials and the substrate, temperature gradient in the tube furnace, source materials, *etc.* Among these experimental parameters, the growth temperature and gas-phase supersaturation are two dominant processing factors while the other experimental parameters play minor roles.[11,31] For the VLS growth mechanism to happen, it has a strict requirement for the growth temperature and gas-phase supersaturation. Otherwise, the VS growth mechanism will take place in the nucleation and growth of low-dimensional nanostructures.

Let us take the growth of ZnO nanostructures in the furnace using a mixture of ZnO and graphite powders as the source materials as an example. The prerequisite for the VLS to occur is the formation of liquid metal alloys. In the previous works, it has been shown that the formation of a Au–Zn alloy droplet frequently requires a process temperature of about 900 °C using a mixture of ZnO and graphite powders as the source materials.[9,37] Hence, if the process temperature is less than 900 °C, it is plausible that the growth of ZnO nanostructures can only be governed by the VS mechanism. At the process temperature around 900 °C or a bit higher, the VLS mechanism will become the dominant one. However, if process temperatures are significantly higher than 900 °C, too high process temperatures can facilitate two-dimensional nucleation and growth of ZnO nanostructures. This means that the VS mechanism will come into play and eventually lead to the complete VS growth mechanism at a very high process temperature.

This discussion also applies to the zinc vapour gas-phase supersaturation. At a too low zinc gas-phase supersaturation, it is very difficult to form Au–Zn liquid alloys. For example, if 5 at% of zinc is dissolved into 95 at% of gold, the formation of a liquid Au–Zn alloy requires a high temperature of 900 °C according to the Au–Zn phase diagram. This means the VS

growth mechanism will play an important role. The VLS growth mechanism will dominate the process until an appropriate zinc vapour-gas supersaturation has been met. Likewise, too high zinc vapour-gas supersaturation can promote two-dimensional nucleation and growth, and eventually the VS growth mechanism will dominate the process. It is noteworthy that, recently, Ramgir et al.[35] have demonstrated a reversible switching between the VS and VLS growth mechanisms by simply changing the zinc vapour-gas supersaturation through adding or removing an ionic liquid.

In this work, we have deliberately chosen a pure zinc powder as a zinc vapour source. This is because the melting point of zinc (420 °C) is significantly lower than that of ZnO (1975 °C). Thereby, the Zn powder is expected to generate a much higher vapour pressure in comparison with the commonly used mixture of ZnO and graphite powders as the source materials under a similar process temperature. As such, it will enable us to control the zinc vapour-phase supersaturation and the formation of Au–Zn liquid alloys in a relatively easy way at a low process temperature. Moreover, the graphite as a reductant to reduce the vaporization temperature of ZnO to 900 °C can often complicate the process. For instance, the role of CO and CO_2 gases (the products of the carbothermal reaction) on the growth of low-dimensional ZnO nanostructures is still controversial. Recently, Subannajui et al.[38] have used numerical modelling and controlled oxygen experiments to reveal that CO and CO_2 gases are not always effective enough to stimulate the growth of low-dimensional ZnO nanostructures while they can enhance the tendency to grow a continuous film. The use of a pure zinc powder as a zinc vapour source in this work enabled us to simplify the growth process (easy to control gas supersaturation, formation of liquid alloys, gas-phase reactions, etc.) and observe the growth mechanism transition between VS and VLS at a relatively low process temperature.

5. Conclusion

In this work, the growth mechanism transition between VS and VLS for the synthesis of low-dimensional ZnO nanostructures has been demonstrated by changing the process temperature via a simple thermal evaporation and vapour-phase transport approach in a conventional horizontal quartz tube furnace using a high-purity Zn powder and oxygen gas as reactants. The detailed growth mechanisms presented here shed light on some controversies about the underlying mechanisms for the growth of low-dimensional ZnO nanostructures. Moreover, the properties of the synthesized low-dimensional ZnO nanostructures were extensively and systematically studied using a broad range of advanced characterization tools. It is shown that these properties can be effectively controlled by the process temperature.

Acknowledgements

References

1 K. Ostrikov, *Rev. Mod. Phys.*, 2005, **77**, 489.
2 H. E. Unalan, P. Hiralal, D. Kuo, B. Parekh, G. Amaratunga and M. Chhowalla, *J. Mater. Chem.*, 2008, **18**, 5909.
3 J. Zheng, R. Yang, L. Xie, J. Qu, Y. Liu and X. Li, *Adv. Mater.*, 2010, **22**, 1451.
4 J. Shieh, F. J. Hou, Y. C. Chen, H. M. Chen, S. P. Yang, C. C. Cheng and H. L. Chen, *Adv. Mater.*, 2010, **22**, 597.
5 U. Cvelbar, K. Ostrikov, I. Levchenko, M. Mozetic and M. K. Sunkara, *Appl. Phys. Lett.*, 2009, **94**, 211502.
6 D. Mariotti and K. Ostrikov, *J. Phys. D: Appl. Phys.*, 2009, **42**, 092002.
7 S. Y. Huang, S. Xu, J. W. Chai, Q. J. Cheng, J. D. Long and K. Ostrikov, *Mater. Lett.*, 2009, **63**, 972.
8 K. Gao, W. Zhang, J. Sun, N. Xu, Z. F. Ying, Q. Li, J. Gan and J. D. Wu, *J. Phys. Chem. C*, 2009, **113**, 19139.
9 M. H. Huang, Y. Wu, H. Feick, N. Tran, E. Weber and P. Yang, *Adv. Mater.*, 2001, **13**, 113.
10 Z. L. Wang, *J. Phys.: Condens. Matter*, 2004, **16**, R829.
11 C. Ye, X. Fang, Y. Hao, X. Teng and L. Zhang, *J. Phys. Chem. B*, 2005, **109**, 19758.
12 J. Rybczynski, D. Banerjee, A. Kosiorek, M. Giersig and Z. F. Ren, *Nano Lett.*, 2004, **4**, 2037.
13 X. Zhong, X. Wu and K. Ostrikov, *Plasma Processes Polym.*, 2009, **6**, 161.
14 N. Wang, Y. Cai and R. Q. Zhang, *Mater. Sci. Eng., R*, 2008, **60**, 1.
15 W. I. Park, D. H. Kim, S. W. Jung and G. C. Yi, *Appl. Phys. Lett.*, 2002, **80**, 4232.
16 Y. Sun, G. M. Fuge and M. N. R. Ashfold, *Superlattices Microstruct.*, 2006, **39**, 33.
17 P. Huh, F. Yan, L. Li, M. Kim, R. Mosurkal, L. A. Samuelson and J. Kumar, *J. Mater. Chem.*, 2008, **18**, 637.
18 D. S. Kim, R. Scholz, U. Gösele and M. Zacharias, *Small*, 2008, **4**, 1615.
19 Q. J. Cheng, S. Xu and K. Ostrikov, *Acta Mater.*, 2010, **58**, 560.
20 Q. J. Cheng, S. Xu and K. Ostrikov, *Nanotechnology*, 2009, **20**, 215606.
21 Q. J. Cheng, S. Xu and K. Ostrikov, *J. Mater. Chem.*, 2009, **19**, 5134.
22 M. Willander, L. L. Yang, A. Wadeasa, S. U. Ali, M. H. Asif, Q. X. Zhao and O. Nur, *J. Mater. Chem.*, 2009, **19**, 1006.
23 S. Li, X. Zhang, B. Yan and T. Yu, *Nanotechnology*, 2009, **20**, 495604.
24 Q. J. Cheng, S. Xu, J. D. Long and K. Ostrikov, *Appl. Phys. Lett.*, 2007, **90**, 173112.
25 H. Koga, T. Kitaoka and H. Wariishi, *J. Mater. Chem.*, 2009, **19**, 2135.
26 J. Zheng, Y. Yang, B. Yu, X. Song and X. Li, *ACS Nano*, 2008, **2**, 134.
27 K. Ostrikov, et al., *Nanoscale*, 2010, **2**, 2012.
28 U. Cvelbar, Z. Q. Chen, M. K. Sunakra and M. Mozetic, *Small*, 2008, **4**, 1610.
29 K. A. Dick, K. Deppert, T. Mårtensson, B. Mandl, L. Samuelson and W. Seifert, *Nano Lett.*, 2005, **5**, 761.
30 C. Geng, Y. Jiang, Y. Yao, X. Meng, J. A. Zapien, C. S. Lee, Y. Lifshitz and S. T. Lee, *Adv. Funct. Mater.*, 2004, **14**, 589.
31 H. Wan and H. E. Ruda, *J. Mater. Sci.: Mater. Electron.*, 2010, **21**, 1014.
32 J. B. Hannon, S. Kodambaka, F. M. Ross and R. M. Tromp, *Nature*, 2006, **440**, 69.
33 L. Cao, B. Garipcan, J. S. Atchison, C. Ni, B. Nabet and J. E. Spanier, *Nano Lett.*, 2006, **6**, 1852.
34 M. Zacharias, K. Subannajui, A. Menzel and Y. Yang, *Phys. Status Solidi B*, 2010, **247**, 2305.
35 N. S. Ramgir, K. Subannajui, Y. Yang, R. Grimm, R. Michiels and M. Zacharias, *J. Phys. Chem. C*, 2010, **114**, 10323.
36 H. J. Fan, W. Lee, R. Hauschild, M. Alexe, G. L. Rhun, R. Scholz, A. Dadgar, K. Nielsch, H. Kalt, A. Krost, M. Zacharias and U. Gösele, *Small*, 2006, **2**, 561.
37 D. Zhao, C. Andreazza, P. Andreazza, J. Ma, Y. Liu and D. Shen, *Chem. Phys. Lett.*, 2004, **399**, 522.
38 K. Subannajui, N. Ramgir, R. Grimm, R. Michiels, Y. Yang, S. Müller and M. Zacharias, *Cryst. Growth Des.*, 2010, **10**, 1585.